Global excitability and network structure in the human brain

Youssef Kora, Salma Salhi, Jörn Davidsen, and Christoph Simon
Department of Physics and Astronomy, University of Calgary, Calgary, Alberta T2N 1N4, Canada
and Hotchkiss Brain Institute, University of Calgary, T2N 4N1 Calgary, Canada

(Received 4 January 2023; accepted 7 April 2023; published 31 May 2023)

We utilize a model of Wilson-Cowan oscillators to investigate structure-function relationships in the human brain by means of simulations of the spontaneous dynamics of brain networks generated through human connectome data. This allows us to establish relationships between the global excitability of such networks and global structural network quantities for connectomes of two different sizes for a number of individual subjects. We compare the qualitative behavior of such correlations between biological networks and shuffled networks, the latter generated by shuffling the pairwise connectivities of the former while preserving their distribution. Our results point towards a remarkable propensity of the brain to achieve a trade-off between low network wiring cost and strong functionality, and highlight the unique capacity of brain network topologies to exhibit a strong transition from an inactive state to a globally excited one.

DOI: 10.1103/PhysRevE.107.054308

I. INTRODUCTION

The human brain is arguably the most complex and inscrutable object in the universe. Constructing a complete theory of its workings has long been considered an impracticable pursuit, but tools such as network analysis allow us to make considerable strides towards that end [1] by modeling the brain as a network of neuronal elements [2] to which the quantitative analysis of graph theory [3] may be applied, and from which theoretical insights into the widely observed neuroscientific phenomena may be obtained. Such is the general framework underlying the emerging field of network neuroscience [4].

The networks employed in this sort of studies are constructed in a coarse-grained manner; the graphs typically comprise tens or hundreds of nodes, each representing a specialized, spatially segregated anatomical brain region. Those graphs in which the edges correspond to the anatomical fiber connections between the different brain regions are known as structural networks, and those in which the edges reflect statistical relationships based on similarity measures between neuronal components are referred to as functional networks [5]. The former are typically extracted from data obtained through such noninvasive techniques as diffusion tensor imaging, and the recent advances therein have allowed for the comprehensive imaging and mapping of the structure of the human brain: The human structural connectome [6–8]. Functional networks, on the other hand, are constructed by measuring patterns of functional activity observed through such techniques as electroencephalography (EEG) and functional magnetic resonance imaging (fMRI), which shed light on the topology of both the spontaneously emergent dynamical patterns and those that manifest themselves during the performance of tasks [9–15].

Connectomes obtained through such neuroimaging techniques, be they structural or functional, are amenable to the drawing of quantitative neuroscientific conclusions. For instance, the identification of nodes with especially strong contributions, known as hubs, may be achieved through a centrality analysis [16], in which the relative importance of different anatomical structures may be estimated by studying their betweenness within the network [17] or by looking at the eigenvector decomposition of the network [18,19].

Such a framework furthermore lends itself to the exploration of one of the central research areas in neuroscience, namely, the study of structure-function relationships. The goal is to understand the emergence of complex neurodynamics underlain by the anatomical structure of the human brain. To that end, much of the research effort in the last two decades [20–28] has drawn upon the theory of dynamical systems, enabling the implementation and simulation of dynamical models constrained by the anatomical network topology [29], thereby allowing the investigation of the profound relationship between structure and function. Prominent examples of such dynamical models that, in principle, allow one to generate functional connectomes from structural ones include neural mass models [30,31], oscillator models [32–36], and spin models [37–41].

We consider one such popular framework, that of Wilson-Cowan oscillators [42], which is a biologically motivated model for the dynamics of neuronal populations. Here, the dynamical state of the brain may be varied by the tuning of a single parameter, the parameter c_5; upon exceeding a certain value c_5^T, the system transitions from an inactive state, where all activity in the network is suppressed and rapidly decays, to a globally excited state, in which a multitude of brain regions exhibit rich oscillatory dynamics. This phenomenon is illustrated with an example in Fig. 1, in which the top panel shows the globally inactive state, wherein all initial activity is bound to dwindle down, and the bottom panel shows the system just beyond the transition, whereupon a preponderance of activity suddenly manifests itself in a myriad of brain regions. The transition value of c_5 at which this phenomenon occurs, which is found to vary across individual subjects [43], may be related to a given brain network's capacity for global excitation; the lower the value of c_5^T, the more easily excitable the system is.

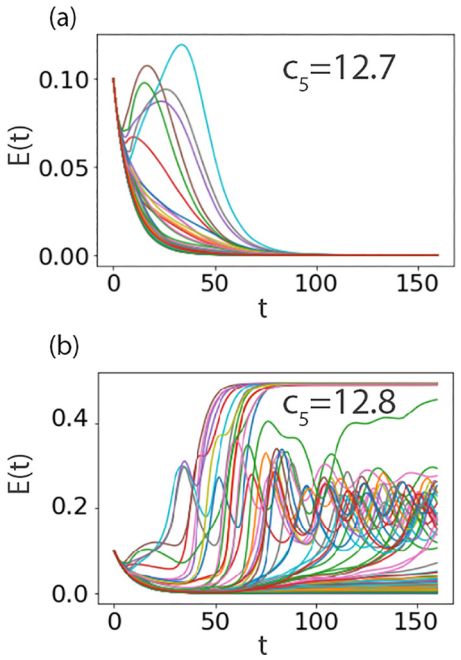

FIG. 1. The dynamics of the proportion of excitatory cells firing per unit time, for subject 111211, at (a) $c_5 = 12.7$ and (b) $c_5 = 12.8$. Each line corresponds to a brain region.

In the past, the Wilson-Cowan model has been used to reproduce the resting state fMRI activity of a simplified network with 38 cortical nodes and 2 subcortical ones [20]. It has also been used to establish a connection between neurodynamics and theories of consciousness [44]. Furthermore, in [45,46], it was found that global excitability, as represented by the value of c_5^T, predicted performance in complex cognitive tasks such as sentence completion. Motivated by these findings, we set out to explore the manner in which the human brain's propensity for global excitation is dependent on the special architecture of the underlying networks. And so by means of implementing the Wilson-Cowan model, we simulated the resting state brain fluctuations within two types of individualized structural connectomes: The first (second) comprising 104 (84) cortical and subcortical structures, referred to henceforth as the extended (restricted) connectome. We explored the relationship between a global functional quantity such as c_5^T and global structural network quantities computed for the structural connectomes, and we investigated the manner in which the transition manifested itself and how it differed between individuals. We also compared the behavior of biological networks to that of randomized networks with identical distributions of connectivities, in order to gain insight into the unique properties of the former.

The remainder of this paper is organized as follows: In Sec. II, we describe our methodology for data extraction and analysis. We present and discuss our results in Sec. III, and finally outline our conclusions in Sec. IV.

II. MATERIALS AND METHODS

A. Model

We employ the form of the Wilson-Cowan model used in Ref. [45]. Underlying the Wilson-Cowan model is the assumption that all neurological processes of interest are governed by the interaction between excitatory and inhibitory cells. It is furthermore assumed that each subpopulation of such cells at every brain region may be characterized by a single variable. Defining E_i and I_i as the respective fractions of excitatory and inhibitory cells firing per unit time in region i, the Wilson-Cowan model reads

$$\tau \frac{dE_i}{dt} = -E_i(t) + [S_{E_m} - E_i(t)]S_E\left[c_1 E_i(t) - c_2 I_i(t) + c_5 \sum_j J_{ij} E_j\left(t - \tau_d^{ij}\right) + P_i(t)\right] + \sigma w_i(t) \tag{1}$$

and

$$\tau \frac{dI_i}{dt} = -I_i(t) + [S_{I_m} - I_i(t)]S_I\left[c_3 E_i(t) - c_4 I_i(t) + c_6 \sum_j J_{ij} I_j\left(t - \tau_d^{ij}\right)\right] + \sigma v_i(t), \tag{2}$$

where $S_{E,I}(x)$ are sigmoid functions given by

$$S_{E,I}(x) = \frac{1}{1 + e^{-a_{E,I}(x - \theta_{E,I})}} - \frac{1}{1 + e^{a_{E,I}\theta_{E,I}}}, \tag{3}$$

and S_{E_m,I_m} are the maxima thereof, and the constants $a_{E,I}$ and $\theta_{E,I}$, respectively, determine the value and position of the maximum slope. J_{ij} refers to the elements of the anatomical connectivity matrix. An external stimulation $P_i(t)$ may be applied to excitatory cells. The finite distance d_{ij} between two brain regions gives rise to the communication delay $\tau_d^{ij} = d_{ij}/v_d$, where $v_d = 10$ m/s is a typical estimate of the signal transmission velocity (see, for instance, Ref. [47]). A normal distribution of noise is added to the system through the functions $w_i(t)$ and $v_i(t)$, with strength σ.

An intuitive understanding of the model may be acquired by considering the second term on the right-hand sides of both equations, which represents the respective activity in each subpopulation, i.e., the proportion of cells which meet the two conditions of (a) being sensitive to an excitation (not in a refractory state) and (b) receiving at least threshold excitation at the same time t. The probability for the former condition is represented by the bracket multiplying the sigmoid function, and the probability for the latter condition is represented by the sigmoid function itself. The choice of the sigmoid

function is fundamentally based on empirical observations of both single cell and population response curves [48,49], but the underlying intuition is straightforward: Too small an excitation will fail to excite any elements at all, whereas a very large one can do no more than excite the entirety of the population. The argument of the sigmoid function is, of course, the excitation itself, which is enhanced by excitatory cells, suppressed by inhibitory ones, contributed towards by the other nodes through the structural connectivity matrix, and potentially by a stimulation $P_i(t)$.

It is standard to use biologically derived values for all the parameters in the model besides c_5 and c_6, which, respectively, represent the excitatory and inhibitory global coupling strengths between all brain regions in the network [50]. As in [45], we set $c_6 = c_5/4$ based on an approximate ratio between excitatory and inhibitory coupling. Thus, c_5 remains the only free parameter and its tuning, as mentioned above, determines the dynamical state of the brain in the model.

B. Structural data

We constrained the Wilson-Cowan dynamical model by the structural connectivity data produced from the 1200 subject cohort of the Human Connectome Project (HCP) [51], a database containing neural data for thousands of subjects, of which we selected a sample for our calculations. The selection was done on no particular basis; we simply chose the first subjects from the 1200 subject HCP database, about which no information was provided besides the age and gender. Both preprocessed T1-weighted structural images and 3T dMRI images were used in our computational fiber tracking method. The PYTHON DIPY and NiBabel libraries were utilized to perform the streamline calculations using a constrained spherical deconvolution model and probabilistic fiber tracking functions, which are built in the libraries.

The product of this procedure was a set of undirected structural connectivity networks, each belonging to an individual subject and comprising 104 nodes corresponding to cortical or subcortical brain structures, the full list of which may be found in Table I in the Appendix. The networks were then normalized by dividing the strength of each connection by the sum of the volumes of its two nodes, as in earlier studies [43,45] (for a comparison with results for non-normalized connectomes, see Fig. 8 in the Appendix.). The matrices representing the physical distances between brain regions were obtained by using the mapping algorithm in our code to determine the coordinates of the nodes and then computing the distances between them, which, in so coarse grained a parcellation of the human brain, were simply approximated as Euclidean distances.

In an effort to investigate the effect of the atlas that was utilized, we also generated restricted connectomes for the same set of subjects, this time with 84 brain regions. The structures excluded from the restricted connectomes include the brainstem among a number of other subcortical regions, the full list of which may be found in Table II in the Appendix. These 84 brain regions constitute the FreeSurfer Desikan-Killiany atlas [52], which is often used in studies relying on the MRTRIX software (see [53] for more details).

Finally, we generated, for each subject, a network with shuffled connectivities, while preserving the overall distribution of connectivities (but not the distribution of degree centralities). This is accomplished by randomly rearranging the entries of the original 104×104 matrix $\mathbf{J}$ below the diagonal, while preserving their numerical values, and then reflecting them about the diagonal to restore the symmetry of the matrix. This allowed us to study the way in which structure-function relationships are affected by the specific arrangement of anatomical connectivities in the brain. To distinguish these shuffled connectomes from the ones obtained from imaging data, we shall henceforth refer to the latter as biological connectomes, be they extended (comprising 104 brain regions) or restricted (comprising 84 brain regions)

C. Network characteristics

A number of global structural properties were computed for each network. The first of these is the characteristic path length, which is a global measure of how strongly connected a network is [54]. It is computed as the average path length between all possible pairs of vertices,

$$L = \frac{1}{N(N-1)} \sum_{i,j \in N, i \neq j} s_{ij}, \tag{4}$$

where N is the number of nodes, and s_{ij} is the shortest distance between nodes i and j (note that this graph-theoretical distance s_{ij} is not to be confused with the physical distance d_{ij}). In the case of weighted graphs such as our own, we computed the distance between two nodes as simply the reciprocal of the strength of the connection between them. i.e., $1/J_{ij}$, and the Dijkstra shortest path [55] s_{ij} was then computed for every pair of nodes. Another closely related measure is the average degree, i.e., the total connectivity of a given node averaged across all nodes, given by

$$K = \frac{1}{N(N-1)} \sum_{i,j \in N} J_{ij}. \tag{5}$$

We also computed the spectral radius R, which is related to the variability of the degrees of nodes [56], and is simply given by the largest eigenvalue of the connectivity matrix. Finally, we computed the synchronizability of the networks, given by $\frac{\lambda_2^L}{\lambda_{\max}^L}$, with λ_2^L and $\lambda_{\max}^L$, respectively, being the second-to-smallest and the largest eigenvalue of the Laplacian matrix $L = D - J$, which is the difference between the degree matrix and the connectivity matrix [57]. This ratio has been shown to determine synchronizability for oscillator networks by assessing the linear stability of the synchronous state [58]. We then measured the correlations of all these structural quantities with the functional quantity c_5^T in an effort to gain insight into structure-function relationships within this framework.

We quantify the degree of hierarchical structure within networks by means of the global reaching centrality (GRC) [59], for which computation we employed the PYTHON package NetworkX [60]. GRC is defined, for a graph G with N nodes, as

$$\mathrm{GRC} = \frac{\sum_{i \in V} \left[C_R^{\max} - C_R(i)\right]}{N-1}, \tag{6}$$

where V is the set of nodes in G, $C_R(i)$ is the local reaching centrality of node i, and $C_R^{\max}$ is the maximum value thereof.

Local reaching centrality is defined for unweighted directed graphs as the fraction of all nodes in the network that may be reached from node i, and generalized for weighted graphs as

$$C_R(i) = \frac{1}{N-1} \sum_{j:0<n^{\text{out}}(i,j)<\infty} \frac{\sum_{k=1}^{n^{\text{out}}(i,j)} w_i^{(k)}(j)}{n^{\text{out}}(i,j)}, \tag{7}$$

with $n^{\text{out}}(i, j)$ being the number of links along the shortest path from node i to node j, and $w_i^{(k)}(j)$ the weight of the kth such link.

Finally, we computed the clustering coefficient, which quantifies the tendency of nodes to cluster together, may be generalized to weighted networks by means of the geometric average of weights [61], and may be computed for a given node as

$$c_i = \frac{1}{k_i(k_i-1)} \sum_{j,k} (J_{ij}J_{ik}J_{jk})^{1/3}, \tag{8}$$

where k_i is the degree of the node. The clustering coefficient of the entire network is simply the average across all its nodes. The PYTHON package NetworkX [60] was also utilized here.

D. Simulation details

The dynamics were simulated using the Wilson-Cowan model, as explained above, in the absence of an external stimulation. We utilized a second-order Runge-Kutta solver with a sufficiently fine time step, such that the results were independent of the size thereof. For each individual subject, the value of c_5^T was estimated by simulating the model at multiple values of c_5 and observing the point at which the transition took place.

We switched off the external stimulation, initialized all oscillators at $E = I = 0.1$, and chose the parameters $\sigma = 10^{-5}$, $c_1 = 16$, $c_2 = 12$, $c_3 = 15$, $c_4 = 3$, $a_E = 1.3$, $a_I = 2$, $\theta_E = 4$, $\theta_I = 3.7$, and $\tau = 8$ as prescribed in the literature [43,45]. At these values of the parameters, the oscillators can be in one of three states: A low fixed point, a high fixed point, and an oscillatory limit cycle in-between [43]. For every subject, we observed the strong transition (as discussed in Sec. I) into a globally excited state, i.e., from a state where activity in all oscillators decays into the low fixed point, to a state where a significant fraction of the oscillators transitions into either the limit cycle or the high fixed point. As mentioned above, this is achieved by varying the global coupling parameter c_5, and the value at which this transition takes place in the absence of an external stimulation, c_5^T, is unique for each subject, at a given choice of parameters and initial conditions. We demonstrate the effect in Fig. 1, which displays the fraction of excitatory cells firing per unit time in each brain region as a function of time for a given subject, and in the absence of an external stimulation.

III. RESULTS AND DISCUSSION

We start by comparing all three types of connectomes (extended, restricted, and shuffled) in Fig. 2, in which we plot for each type of connectome the transition value c_5^T vs the characteristic path length L. Each of the six different symbols corresponds to a different subject. A few things may be noted

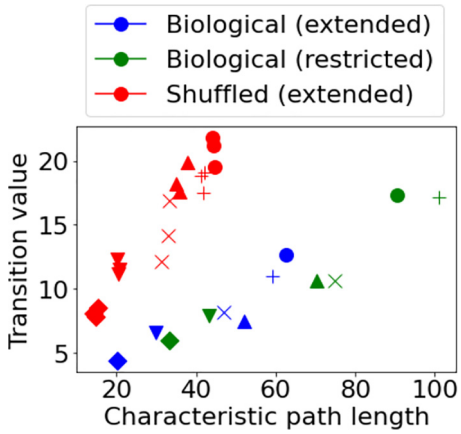

FIG. 2. The transition value c_5^T vs the characteristic path length of a network. Symbol shapes correspond to individual subjects. Blue symbols are extended connectomes, green are restricted connectomes (in accordance with the FreeSurfer Desikan-Killiany atlas [52]), and red are extended connectomes with randomly redistributed connectivities (preserving the overall distribution of connectivities). Errors are smaller than the symbol sizes.

by observing Fig. 2. First, both sorts of biological networks fall on the same trend line ($r^2 = 0.879$). This is a simple observation that more strongly connected networks (shorter characteristic path length) have a higher tendency for global excitation (lower transition value) [62].

Second, by comparing the green points (corresponding to the FreeSurfer Desikan-Killany atlas [52]) to the blue points in Fig. 2, one observes that the restricted network for any given subject invariably has a higher characteristic path length and higher transition value than its extended counterpart. This suggests that the exclusion of the brainstem (and the other 19 structures absent from the FreeSurfer Desikan-Killiany atlas [52]) causes the networks to be substantially less well connected, and thus harder to globally excite. This observation is consistent with the findings in [53], highlighting the structural importance of the brainstem, and of incorporating the full list of subcortical structures. We eliminated the possibility that this difference is an artifact of the system size by performing the same calculations for another set of restricted connectomes with 20 excluded structures, but now with the latter's being randomly chosen. The list of such structures, the same for every subject, may be found in Table III in the Appendix, and the result of the analysis may be found in Fig. 9 and the associated text, also in the Appendix.

The third observation is perhaps the most striking. It is clear that shuffling the connectivities of extended networks (as represented by the red points in Fig. 2) invariably shortens the characteristic path length while causing the transition value to rise, which causes the red points to deviate from the biological trend line. Instead, the random networks form their own displaced trend line. We find it rather curious, not only that a biological network should always be less strongly connected compared to a random network with the same distribution of connectivities, but that it should simultaneously have a higher global excitability. This is the reverse of the phenomenon observed upon excluding the 20 subcortical structures (going

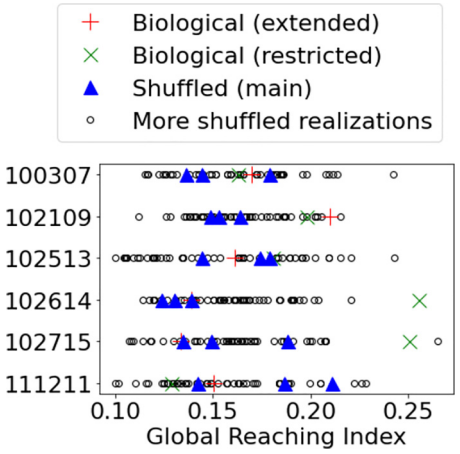

FIG. 3. The global reaching centrality of the biological extended (red pluses) and biological restricted (green x's), the three main realizations of shuffled networks (blue triangles), and 50 more realizations of the latter (black hollow circles). The results are presented for six subjects.

from the blue points to the green points), which caused the networks to both be less well connected and less globally excitable. For alternative presentations of the data in Fig. 2, respectively, in terms of the reciprocals of the axes and the clustering coefficient, see Figs. 10 and 11 in the Appendix.

The tendency of random networks to have a low characteristic path length is, by itself, an unsurprising finding, as random networks tend to have a low mean path length [3,54]. However, that global excitability should fall in spite of that is quite an interesting observation and has implications for the economics of brain network organization. The creation and maintenance of anatomical connections is an expensive affair, and the brain must therefore sagaciously utilize resources within the network in order to bring about the desired topological properties in an efficient way [63]. Consistent with this trade-off principle, the results in Fig. 2 suggest that brain networks are wired in a manner that is both parsimonious and uncompromising of the required topology for high global excitability. As a possible underlying cause for this disparity in behavior between biological and shuffled networks, one candidate is the hierarchical structure of biological networks [64,65]. In particular, it has been demonstrated that the hierarchical manner in which connectivity is distributed within the human connectome is responsible for giving rise to critical dynamics over an extended region of parameter space, known as the Griffiths phase, rather than a singular critical point (see, for instance, Refs. [66–68]). There are a number of ways to quantify the extent of hierarchy within a network [59,69], which allow us to test the hypothesis that these hierarchies are largely preserved in going from the biological extended connectome to the biological restricted one, but are destroyed when pairwise connectivities are randomly shuffled. Specifically, to investigate this hypothesis, we computed the global reaching centrality (GRC) (defined in Sec. II C) for the biological extended connectome, the restricted one, the three realizations of shuffling presented earlier, and 50 additional realizations of shuffling. The results, presented in Fig. 3 for six different subjects, suggest that the shuffling

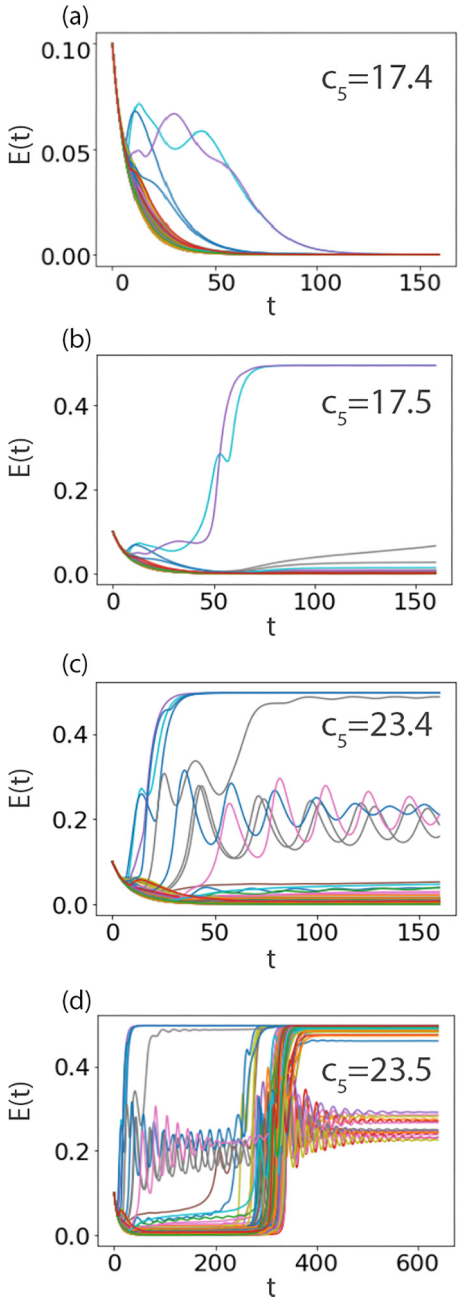

FIG. 4. The dynamics of the excitatory firing rates of the shuffled network of subject 111211, at (a) $c_5 = 17.4$, (b) $c_5 = 17.5$, (c) $c_5 = 23.4$, and (d) 23.5. Here, $c_5^T = 23.4$.

process does not, in general, tend to degrade the hierarchical structure of the biological connectomes, at least not within our rather coarse-grained connectomes. Thus, our GRC analysis indicates that the high global excitability in our human brain connectomes is not due to any hierarchical architecture. Another notable difference between biological and shuffled networks is in the manner in which the transition manifests itself. This becomes clear by comparing Figs. 1 and 4. In the former case, there is a sudden, rather dramatic increase of activity upon exceeding the transition value. In the latter case of shuffled networks, this is not always true. Instead, two transitions might be present: At low values of c_5, a transition

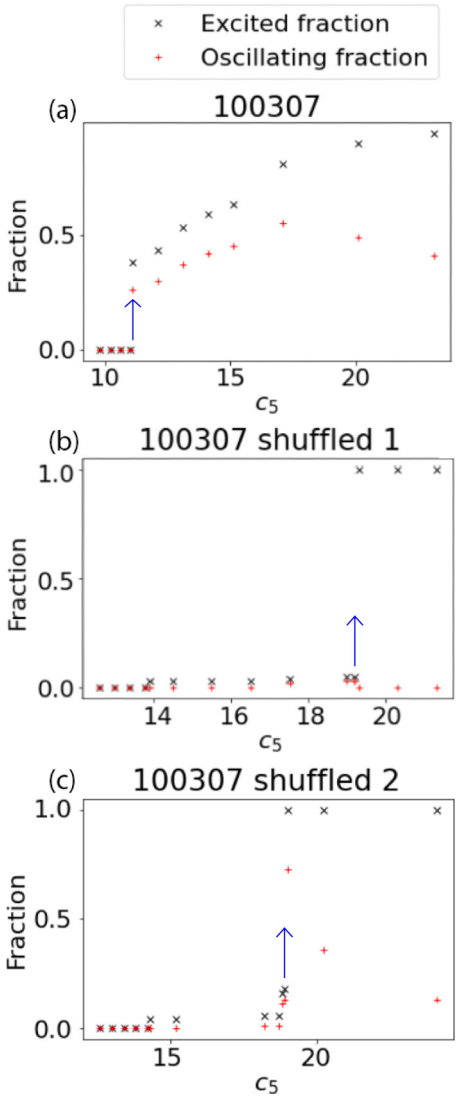

FIG. 5. (a) The excited fraction (crosses) and oscillating fraction (plus) of brain regions for the biological network and (b),(c) two instances of shuffling for that same network belonging to subject 100307. Blue arrows indicate the location of the transition.

occurs to a state where only a very small fraction of brain regions are excited, and then at a sufficiently high value of c_5, an abrupt jump in activity occurs, similar to the biological networks, which is, hence, denoted as c_5^T (for an analysis with c_5^T alternatively defined, see Fig. 12 and associated text in the Appendix).

This phenomenon may also be observed in Fig. 5, which presents the evolution of the excited fraction (the total fraction of brain regions that saturate at the high fixed point or the limit cycle) and the oscillatory fraction (the fraction that includes only those brain regions that saturate at the limit cycle). In all cases, the excited fraction starts at zero at low values of c_5, and saturates to unity at sufficiently high values of c_5. The differences, however, are in the manner in which the excited fraction evolves from zero to unity. In biological networks, we invariably observed a well-defined jump from zero to a finite value of the excited fraction at a specific value of c_5, to which we refer as c_5^T, and beyond which the excited

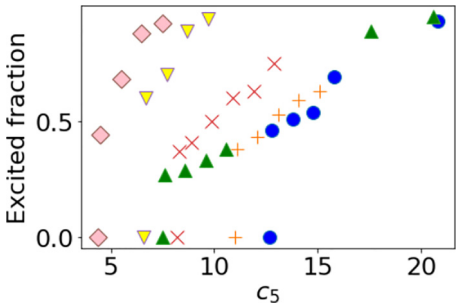

FIG. 6. The excited fraction as a function of c_5. Symbol shapes and colors correspond to subject names. Errors are smaller than symbol sizes.

fraction proceeds to smoothly grow until it saturates at unity. A typical example of this behavior is presented in Fig. 5(a). The situation in shuffled networks is quite different, however; the excited fraction initially starts at zero and, as we raise the value of c_5, the system might leave the unexcited ground state at a certain value of c_5 but manifesting excitations in only a very small fraction of brain regions, until a sufficiently high value of c_5 (which, as previously mentioned, we define as c_5^T) is reached, whereupon *all* brain regions become excited and remain as such as we further increase c_5. This region of meager activity that precedes the transition was often (but not always) observed in shuffled networks and was never seen in any of the biological networks examined. The jump at c_5^T, however, which takes the system from zero (or near zero) to unity, was observed in all realizations of shuffled networks. This behavior may be observed in Figs. 5(b) and 5(c), which present the behavior for two instances of shuffling for the same network.

The behavior of shuffled networks is, however, quite variable. For example, the two realizations of shuffling presented in Figs. 5(b) and 5(c), respectively, show clear differences in the behavior of the oscillatory fraction. It is clear that in the case of the shuffled network in Fig. 5(b), the oscillatory fraction never gains a significant value at any point, even after the transition takes place at $c_5^T = 19.2$. This is in clear contrast to the case in Fig. 5(c), in which a significant fraction of brain regions exhibits nontrivial oscillations beyond the transition, albeit rapidly decaying as we further raise the value of c_5. These qualitatively different classes of behavior suggest that the specific way in which anatomical connections are arranged in the brain is crucial for guaranteeing a strong transition into a state with prolific oscillatory dynamics as exhibited in Fig. 5(a).

We also conducted a closer inspection of the manner in which the transition manifests itself in the case of biological networks and how it varies across individuals. In Fig. 6, we plot the excited fraction as a function of c_5 for each of the six subjects considered in this study. Every biological network experienced a considerable jump in the excited fraction upon crossing its respective value of c_5^T, as mentioned above. But not only was the size of the jump different across subjects and seemingly uncorrelated with the value of c_5^T, but so was the rate at which the excited fraction continued to grow. This demonstrates that individual variability across subjects is not limited to the value of c_5^T itself, but that the character of the

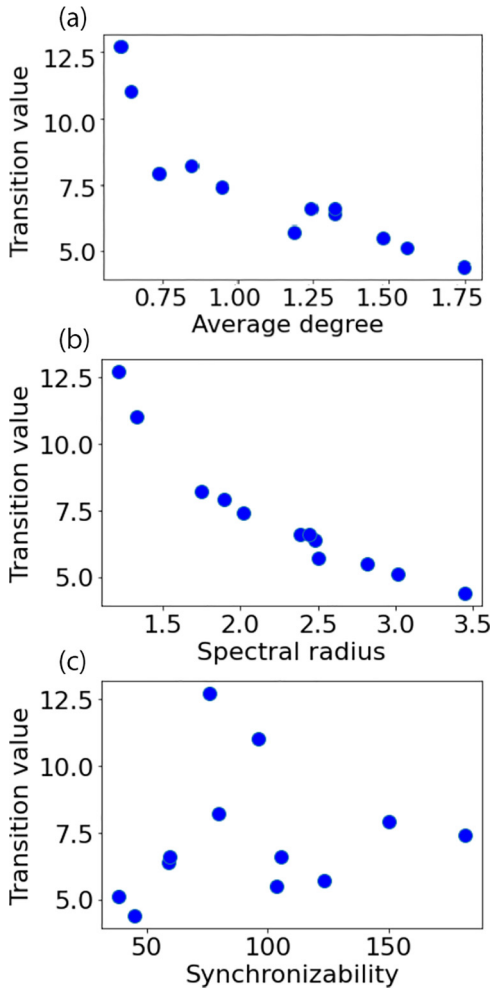

FIG. 7. The transition value c_5^T vs (a) the average degree, (b) spectral radius, and (c) synchronizability, for the six subjects previously considered, in addition to six others. The values of r^2 are, respectively, 0.796, 0.885, and 0.0262.

states beyond the transition, as viewed by studying the growth of the excited fraction, is another independent consideration.

Finally, we measured the correlation between c_5^T and a variety of structural quantities (defined in Sec. II C) and present them in Fig. 7. The average degree and spectral radius are both measures of the overall connectivity of the network, and thus it was not unexpected that they should negatively correlate with the transition value ($r^2 = 0.796, 0.885$, respectively), in light of the result presented in Fig. 2. The difference, however, between the average degree and the spectral radius is that the former is invariant under the shuffling of connectivities, while the latter is not. Last, there was no correlation to be found with global synchronizability ($r^2 = 0.0899$). The latter observation, which suggests that path length and synchronizability are not directly related concepts, is consistent with the "paradox of heterogeneity," which is the observation that (unweighted and undirected) graphs with homogeneous connectivity distributions tend to synchronize more readily than those with heterogeneous ones, irrespective of the latter's possession of lower average path lengths [54,70].

IV. CONCLUSIONS

We studied the spontaneous functional activity that arises in individual brain networks, each belonging to a different subject, by using the Wilson-Cowan model to simulate the network dynamics in the absence of an external stimulation. Under this framework, the dynamical state of the brain is dictated by the numerical value of a single parameter c_5, and at a critical value thereof, referred to as c_5^T, these biological networks exhibit a strong transition from a state where no activity is allowed to propagate to a globally excited state with rich oscillatory dynamics spanning a significant fraction of brain regions. Our results confirm that the value of c_5^T displays significant variability across individuals, and further show that this variability extends to the character of the transition as observed from the behavior of the excited fraction as a function of c_5. We have also drawn insights into the remarkable ability of the brain to comprise networks designed in a manner that is both resource efficient and conducive to the desirable functional properties: Our observations suggest that biological networks form their connectivities so judiciously as to give rise to high global excitability while simultaneously attempting to keep the associated wiring cost reasonably low. Furthermore, it was clear that an invariably strong transition from a globally inactive one to one with ubiquitous oscillatory dynamics is a special property of biological networks, and is, in general, not enjoyed by their shuffled counterparts. We also established correlations between c_5^T and a number of network properties such as characteristic path length, average degree, and spectral radius, but found it to be uncorrelated with network synchronizability. Finally, our results indicate that utilizing a restricted atlas of the human brain causes the networks to become both less well connected and less susceptible to global excitation, in a manner consistent with the biological relationship we established between c_5^T and the characteristic path length.

A possible extension of this work may involve the investigation of the frequencies of the oscillations that manifest themselves at high c_5^T. At first glance, it may seem that these frequencies are brain-region dependent, in addition to being dependent on the value of c_5 itself. It may be worthwhile to investigate how they vary in the brain regions possessing the highest centralities, explore intersubject variability and how the underlying structure affects those differences, or examine them in the context of applied external stimulations.

Another possible extension might be to attempt to connect these results to the critical brain hypothesis, which states that the brain self-tunes to a regime with a large dynamical range that is reminiscent of a critical point or regime in statistical physics [66,71]. Indeed, using the Ising model at its critical point, a recent study has calculated the dimensionality of the brain and found it to vary between healthy groups and those with disorders of consciousness [40]. More fundamentally, the critical brain hypothesis is partially based on the observation of scale-free information or spreading cascades, so-called neuronal avalanches, across species and spatial scales [72–75]. Recent theoretical work suggests that scale-free neuronal avalanches require an "edge-of-synchronization" phase transition [76]. Our work here further suggests that c_5^T could serve as this phase transition point, but more work is needed to explore this in the future.

Our results could also be examined within the context of popular theories of consciousness. Global workspace theory (GWT) is one such theory which suggests that the brain has a fleeting memory capacity, enabling back and forth access between separate brain functions [77]. Specifically, this theory purports that the global network is activated nonlinearly, through a process known as "ignition" [78], which is the sudden activation of neurons that code for current conscious content [79]. It has been shown that a reduction in the interconnectivity of global network neurons makes ignition more difficult to reach [79], suggesting that GWT requires a network that is optimized for high excitability. Another popular theory is integrated information theory (IIT), which identifies and attempts to quantify the capacity of a network to integrate information [80], represented by the quantity Φ, often referred to as the quantity of conscious experience. In [81], Φ was computed for small Ising systems and was found to exhibit criticality at the temperature of the Ising phase transition. While different in their approach, both theories require an efficient functional network. Our results, which suggest that biological networks are uniquely designed to possess great global excitability and strongly transition from an inactive state to a state with rich oscillatory dynamics, could be used to further analyze these theories and shed more light on the mechanism of consciousness.

In summary, we view the main result of the present work to be the observation of the special ability of biological networks to be highly excitable compared to their shuffled counterparts, while simultaneously being less well connected. This high excitability is represented by a reduced value of c_5^T, which has also been observed, in past works, to predict some cognitive measures such as response time to certain tasks [45,46]. We believe this to be a significant result, as it points to the judiciousness of the brain in giving rise to networks imbued with high excitability, while keeping the associated wiring cost under control. It also has potential implications for a variety of topics of interdisciplinary interest, such as network neuroscience, the critical brain hypothesis, and theories of consciousness.

The data used in this project were provided by the Human Connectome Project (HCP; Principal Investigators: Bruce Rosen, M.D., Ph.D., Arthur W. Toga, Ph.D., Van J. Weeden, M.D.) [51]. HCP funding was provided by the National Institute of Dental and Craniofacial Research (NIDCR), the National Institute of Mental Health (NIMH), and the National Institute of Neurological Disorders and Stroke (NINDS). HCP data are disseminated by the Laboratory of Neuro Imaging at the University of Southern California. Structural and diffusion MRI images from the HCP, as well as lists of extracted structures, bvals, and bvecs, were all used to process the data in our PYTHON program. All subjects are part of the "WU-Minn HCP Data - 1200 Subjects" dataset [82]. A complete list of subject names is available upon request. All scripts used to generate the connectomes are available on our Github repository [83].

ACKNOWLEDGMENTS

This work was supported by the Natural Sciences and Engineering Research Council (NSERC) of Canada and the Alberta Major Innovation Fund. We would also like to thank

TABLE I. A full list of the 104 brain structures.

ID	Structure
1	Left-Lateral-Ventricle
2	Left-Inf-Lat-Vent
3	Left-Cerebellum-Cortex
4	Left-Thalamus-Proper
5	Left-Caudate
6	Left-Putamen
7	Left-Pallidum
8	3rd-Ventricle
9	4th-Ventricle
10	Brain-Stem
11	Left-Hippocampus
12	Left-Amygdala
13	CSF
14	Left-Accumbens-area
15	Left-VentralDC
16	Left-vessel
17	Left-choroid-plexus
18	Right-Lateral-Ventricle
19	Right-Inf-Lat-Vent
20	Right-Cerebellum-Cortex
21	Right-Thalamus-Proper
22	Right-Caudate
23	Right-Putamen
24	Right-Pallidum
25	Right-Hippocampus
26	Right-Amygdala
27	Right-Accumbens-area
28	Right-VentralDC
29	Right-vessel
30	Right-choroid-plexus
31	Optic-Chiasm
32	CC_Posterior
33	CC_Mid_Posterior
34	CC_Central
35	CC_Mid_Anterior
36	CC_Anterior
37	ctx-lh-bankssts
38	ctx-lh-caudalanteriorcingulate
39	ctx-lh-caudalmiddlefrontal
40	ctx-lh-cuneus
41	ctx-lh-entorhinal
42	ctx-lh-fusiform
43	ctx-lh-inferiorparietal
44	ctx-lh-inferiortemporal
45	ctx-lh-isthmuscingulate
46	ctx-lh-lateraloccipital
47	ctx-lh-lateralorbitofrontal
48	ctx-lh-lingual
49	ctx-lh-medialorbitofrontal
50	ctx-lh-middletemporal
51	ctx-lh-parahippocampal
52	ctx-lh-paracentral
53	ctx-lh-parsopercularis
54	ctx-lh-parsorbitalis
55	ctx-lh-parstriangularis
56	ctx-lh-pericalcarine
57	ctx-lh-postcentral
58	ctx-lh-posteriorcingulate
59	ctx-lh-precentral

TABLE I. (*Continued.*)

ID	Structure
60	ctx-lh-precuneus
61	ctx-lh-rostralanteriorcingulate
62	ctx-lh-rostralmiddlefrontal
63	ctx-lh-superiorfrontal
64	ctx-lh-superiorparietal
65	ctx-lh-superiortemporal
66	ctx-lh-supramarginal
67	ctx-lh-frontalpole
68	ctx-lh-temporalpole
69	ctx-lh-transversetemporal
70	ctx-lh-insula
71	ctx-rh-bankssts
72	ctx-rh-caudalanteriorcingulate
73	ctx-rh-caudalmiddlefrontal
74	ctx-rh-cuneus
75	ctx-rh-entorhinal
76	ctx-rh-fusiform
77	ctx-rh-inferiorparietal
78	ctx-rh-inferiortemporal
79	ctx-rh-isthmuscingulate
80	ctx-rh-lateraloccipital
81	ctx-rh-lateralorbitofrontal
82	ctx-rh-lingual
83	ctx-rh-medialorbitofrontal
84	ctx-rh-middletemporal
85	ctx-rh-parahippocampal
86	ctx-rh-paracentral
87	ctx-rh-parsopercularis
88	ctx-rh-parsorbitalis
89	ctx-rh-parstriangularis
90	ctx-rh-pericalcarine
91	ctx-rh-postcentral
92	ctx-rh-posteriorcingulate
93	ctx-rh-precentral
94	ctx-rh-precuneus
95	ctx-rh-rostralanteriorcingulate
96	ctx-rh-rostralmiddlefrontal
97	ctx-rh-superiorfrontal
98	ctx-rh-superiorparietal
99	ctx-rh-superiortemporal
100	ctx-rh-supramarginal
101	ctx-rh-frontalpole
102	ctx-rh-temporalpole
103	ctx-rh-transversetemporal
104	ctx-rh-insula

Wilten Nicola, Davor Curic, and Omid Khajehdehi from the Complexity Science Group (CSG) for the discussion and input. Additionally, we thank the HCP for providing access to their data.

APPENDIX

1. Lists of brain regions

Table I lists the 104 structures constituting the extended connectome. Table II lists the 84 structures constituting the restricted connectome. Table III lists the 20 structures removed from the extended connectome to give rise to the restricted one.

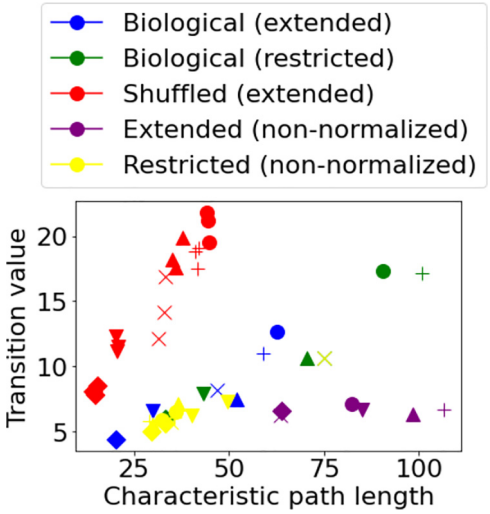

FIG. 8. The same as Fig. 2, but with the inclusion of data points for non-normalized networks, i.e., networks in which edge weights were not divided by the sum of the volumes of their nodes.

2. Supplemental figures

Figure 8 presents the analysis that incorporates connectomes which are not normalized, i.e., the connectivities are not divided by the sum of the volumes of the nodes. It is clear that the yellow points (representing the results for the restricted connectomes) fall on the biological trend line, but the purple points (representing the results for the extended connectomes) do not. The anomalous behavior of the latter is attributable to the presence of exceedingly dominant nodes such as the brainstem, the effect of which is regularized when their great size is taken into account in the normalized connectomes.

Figure 9 compares the biological extended and restricted connectomes to another case of a restricted connectome in

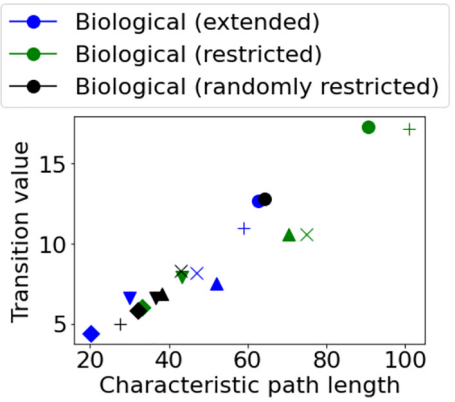

FIG. 9. The transition value c_5^T vs the characteristic path length of a network. Symbol shapes correspond to subject names. Blue symbols are extended connectomes, green are restricted connectomes (in accordance with the FreeSurfer Desikan-Killiany atlas [52]), and black are connectomes restricted by removing 20 randomly chosen regions (found in Table III). Errors are smaller than symbol sizes.

TABLE II. The list of 20 structures removed in the restricted connectome corresponding to the FreeSurfer Desikan-Killiany atlas [52].

Removed structures
Left-Lateral-Ventricle
Left-Inf-Lat-Vent
3rd-Ventricle
4th-Ventricle
Brain-Stem
CSF
Left-VentralDC
Left-vessel
Left-choroid-plexus
Right-Lateral-Ventricle
Right-Inf-Lat-Vent
Right-VentralDC
Right-vessel
Right-choroid-plexus
Optic-Chiasm
CC_Posterior
CC_Mid_Posterior
CC_Central
CC_Mid_Anterior
CC_Anterior

which the excluded structures are chosen randomly, rather than in line with the Desikan-Killiany atlas [52]. One readily observes that while the green points (which correspond to the Desikan-Killiany atlas [52]) are invariably further from the origin than their blue counterparts (corresponding to the extended connectomes) for each and every subject, the same is not true for the black points (corresponding to the randomly restricted connectomes) as compared with their blue counterparts. Indeed, for some subjects, the randomly restricted connectome is more well connected and more highly susceptible to global excitation, and for some other subjects, the converse is true. This suggests that the differences observed between the extended connectome and that which is restricted in accordance with the FreeSurfer Desikan-Killiany atlas [52] are not purely caused by the lower system size of the latter, but rather by the exclusion of too important a set of structures.

TABLE III. The list of 20 structures removed in the randomly restricted connectome.

Removed structures
ctx-lh-middletemporal
ctx-lh-caudalmiddlefrontal
ctx-rh-pericalcarine
ctx-rh-bankssts
Left-VentralDC
ctx-lh-transversetemporal
ctx-lh-cuneus
Left-Inf-Lat-Vent
ctx-lh-frontalpole
ctx-lh-paracentral
Optic-Chiasm
ctx-lh-fusiform
Left-Amygdala
ctx-rh-transversetemporal
ctx-lh-precuneus
ctx-lh-rostralanteriorcingulate
Left-Pallidum
ctx-rh-inferiorparietal
ctx-rh-rostralanteriorcingulate
ctx-lh-insula

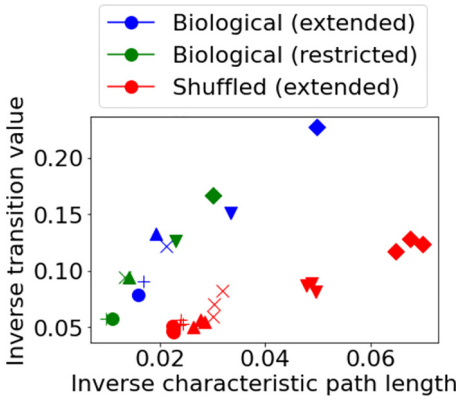

FIG. 10. The same as Fig. 2, but with the reciprocal of the transition value plotted vs the reciprocal of the characteristic path length.

Figure 10 recasts the analysis in Fig. 2 in terms of the reciprocals of the transition value and the characteristic path length. This alternative but equivalent way of presenting the

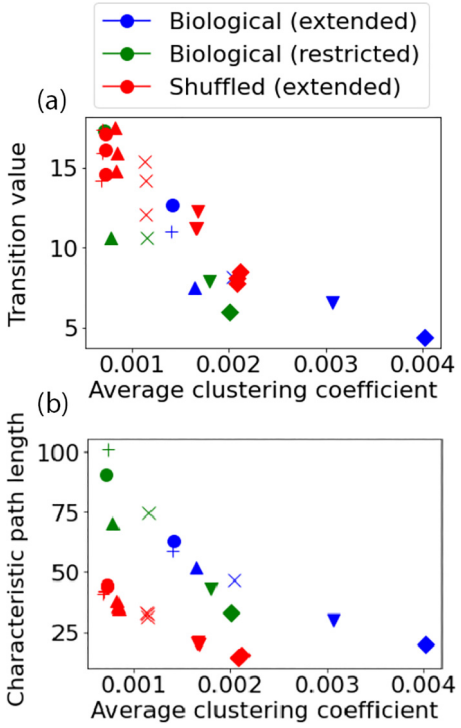

FIG. 11. (a) The transition value c_5^T vs the average clustering coefficient of a network and (b) the characteristic path length vs the average clustering coefficient. Symbol shapes correspond to subject names. Blue symbols are extended connectomes and green symbols are restricted connectomes (in accordance with the FreeSurfer Desikan-Killiany atlas [52]). Errors are smaller than symbol sizes.

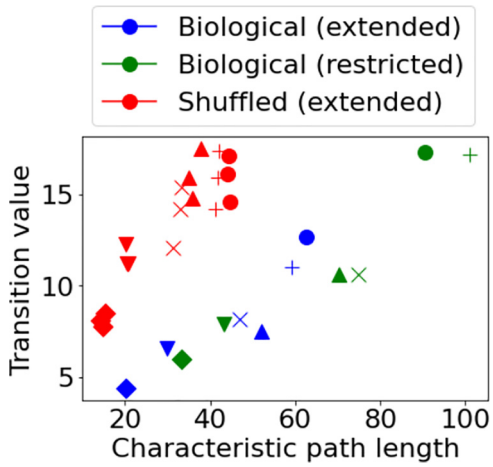

FIG. 12. The same as Fig. 2, but with c_5^T alternatively defined for the shuffled networks to be the lowest value of c_5^T at which the system leaves the ground state, no matter how small the activity.

physics has the advantage of possibly being more intuitive, as the reciprocal quantities are directly related to the global excitability and the overall connectivity, rather than inversely.

Figure 11(a) presents the transition value c_5^T plotted against the average clustering coefficient. It shows that in both sorts of biological networks, it rather strongly anticorrelates with c_5^T, with values of r^2 of 0.873 and 0.969 for the extended and restricted connectomes, respectively. This was hardly a surprising finding, as the clustering coefficient had been observed to anticorrelate with the characteristic path length, as shown in Fig. 11(b). These properties are consistent with a small-world topology [84].

Finally, Fig. 12 presents the case in which we alternatively choose to define c_5^T as the smallest value of c_5 at which the system departs from the ground state (no matter how meager the departure). A comparison with Fig. 2 reveals that the only change is a slight lowering of the slope of the line of red points in Fig. 12 with respect to those in Fig. 2, leaving our conclusions qualitatively unchanged.

[1] O. Sporns, Network analysis, complexity, and brain function, Complexity **8**, 56 (2003).

[2] A. Zalesky, A. Fornito, and E. T. Bullmore, Network-based statistic: Identifying differences in brain networks, NeuroImage **53**, 1197 (2010).

[3] E. Bullmore and O. Sporns, Complex brain networks: Graph theoretical analysis of structural and functional systems, Nat. Rev. Neurosci. **10**, 186 (2009).

[4] D. S. Bassett and O. Sporns, Network neuroscience, Nat. Neurosci. **20**, 353 (2017).

[5] E. W. Lang, A. M. Tomé, I. R. Keck, J. M. Górriz-Sáez, and C. G. Puntonet, Brain connectivity analysis: A short survey, Comput. Intell. Neurosci. **2012**, 1 (2012).

[6] S. Jbabdi, S. N. Sotiropoulos, S. N. Haber, D. C. Van Essen, and T. Behrens, Measuring macroscopic brain connections in vivo, Nat. Neurosci. **18**, 1546 (2015).

[7] Y. Shi and A. W. Toga, Connectome imaging for mapping human brain pathways, Molec. Psychiatry **22**, 1230 (2017).

[8] P. Hagmann, O. Sporns, N. Madan, L. Cammoun, R. Pienaar, V. J. Wedeen, R. Meuli, J.-P. Thiran, and P. E. Grant, White matter maturation reshapes structural connectivity in the late developing human brain, Proc. Natl. Acad. Sci. USA **107**, 19067 (2010).

[9] V. M. Eguíluz, D. R. Chialvo, G. A. Cecchi, M. Baliki, and A. V. Apkarian, Scale-Free Brain Functional Networks, Phys. Rev. Lett. **94**, 018102 (2005).

[10] M. Heuvel, C. Stam, M. Boersma, and H. Hulshoff Pol, Small-world and scale-free organization of voxel-based resting-state functional connectivity in the human brain, NeuroImage **43**, 528 (2008).

[11] S. Hayasaka and P. J. Laurienti, Comparison of characteristics between region- and voxel-based network analyses in resting-state fMRI data, NeuroImage **50**, 499 (2010).

[12] M. E. Raichle, A paradigm shift in functional brain imaging, J. Neurosci. **29**, 12729 (2009).

[13] Z. Rezaei, Z. Jafari, N. Afrashteh, R. Torabi, S. Singh, B. Kolb, J. Davidsen, and M. Mohajerani, Prenatal stress dysregulates resting-state functional connectivity and sensory motifs, Neurobiol. Stress **15**, 100345 (2021).

[14] I. Oliver, J. Hlinka, J. Kopal, and J. Davidsen, Quantifying the variability in resting-state networks, Entropy **21**, 882 (2019).

[15] E. A. Martin, J. Hlinka, and J. Davidsen, Pairwise network information and nonlinear correlations, Phys. Rev. E **94**, 040301(R) (2016).

[16] M. P. van den Heuvel and O. Sporns, Network hubs in the human brain, Trends Cognitive Sci. **17**, 683 (2013).

[17] L. C. Freeman, A Set of Measures of centrality based on betweenness, Sociometry **40**, 35 (1977).

[18] P. Bonacich, Factoring and weighting approaches to status scores and clique identification, J. Math. Sociol. **2**, 113 (1972).

[19] P. Bonacich, Some unique properties of eigenvector centrality, Soc. Networks **29**, 555 (2007).

[20] G. Deco, V. Jirsa, A. R. McIntosh, O. Sporns, and R. Kötter, Key role of coupling, delay, and noise in resting brain fluctuations, Proc. Natl. Acad. Sci. USA **106**, 10302 (2009).

[21] K. J. Friston, Bayesian estimation of dynamical systems: An application to fMRI, NeuroImage **16**, 513 (2002).

[22] K. E. Stephan, On the role of general system theory for functional neuroimaging, J. Anat. **205**, 443 (2004).

[23] S. Makni, C. Beckmann, S. Smith, and M. Woolrich, Bayesian deconvolution fMRI data using bilinear dynamical systems, Neuroimage **42**, 1381 (2008).

[24] U. Sümbül, J. M. Santos, and J. M. Pauly, Improved time series reconstruction for dynamic magnetic resonance imaging, IEEE Trans. Med. Imag. **28**, 1093 (2009).

[25] S. J. Hanson, A. D. Gagliardi, and C. Hanson, Solving the brain synchrony eigenvalue problem: Conservation of temporal dynamics (fMRI) over subjects doing the same task, J. Comput. Neurosci. **27**, 103 (2009).

[26] I. Merlet, G. Birot, R. Salvador, B. Molaee-Ardekani, A. Mekonnen, A. Soria-Frish, G. Ruffini, P. C. Miranda, and F.

Wendling, From oscillatory transcranial current stimulation to scalp EEG changes: A biophysical and physiological modeling study, PLoS ONE **8**, e57330 (2013).

[27] G. Deco, A. Ponce-Alvarez, P. Hagmann, G. L. Romani, D. Mantini, and M. Corbetta, How local excitationinhibition ratio impacts the whole brain dynamics, J. Neurosci. **34**, 7886 (2014).

[28] G. Deco, G. Tononi, M. Boly, and M. L. Kringelbach, Rethinking segregation and integration: Contributions of whole-brain modelling, Nat. Rev. Neurosci. **16**, 430 (2015).

[29] A. E. Motter, M. A. Matías, J. Kurths, and E. Ott, Dynamics on complex networks and applications, Physica D **224**, vii (2006).

[30] O. David, D. Cosmelli, and K. Friston, Evaluation of different measures of functional connectivity using a neural mass model, NeuroImage **21**, 659 (2004).

[31] C. J. Honey, O. Sporns, L. Cammoun, X. Gigandet, J. P. Thiran, R. Meuli, and P. Hagmann, Predicting human resting-state functional connectivity from structural connectivity, Proc. Natl. Acad. Sci. USA **106**, 2035 (2009).

[32] M. G. Kitzbichler, M. L. Smith, S. R. Christensen, and E. Bullmore, Broadband criticality of human brain network synchronization, PLoS Comput. Biol. **5**, e1000314 (2009).

[33] M. Breakspear, S. Heitmann, and A. Daffertshofer, Generative models of cortical oscillations: Neurobiological implications of the Kuramoto model, Front. Hum. Neurosci. **4**, 190 (2010).

[34] B. Yan and P. Li, The emergence of abnormal hypersynchronization in the anatomical structural network of human brain, NeuroImage **65**, 34 (2013).

[35] J. Cabral, H. Luckhoo, M. Woolrich, M. Joensson, H. Mohseni, A. Baker, M. L. Kringelbach, and G. Deco, Exploring mechanisms of spontaneous functional connectivity in MEG: How delayed network interactions lead to structured amplitude envelopes of band-pass filtered oscillations, NeuroImage **90**, 423 (2014).

[36] G. Ódor and J. Kelling, Critical synchronization dynamics of the Kuramoto model on connectome and small world graphs, Sci. Rep. **9**, 19621 (2019).

[37] D. Fraiman, P. Balenzuela, J. Foss, and D. R. Chialvo, Ising-like dynamics in large-scale functional brain networks, Phys. Rev. E **79**, 061922 (2009).

[38] D. Marinazzo, M. Pellicoro, G.-R. Wu, L. Angelini, J. M. Cortes, and S. Stramaglia, Information transfer and criticality in the Ising model on the human connectome, PLoS ONE **9**, e93616 (2014).

[39] P. M. Abeyasinghe, D. R. de Paula, H. Khajehabdollahi, S. R. Valluri, A. M. Owen, and A. Soddu, Role of dimensionality in predicting the spontaneous behavior of the brain using the classical Ising model and the Ising model implemented on a structural connectome, Brain Connect. **8**, 444 (2018).

[40] P. M. Abeyasinghe, M. Aiello, E. Nichols, C. Cavaliere, S. Fiorenza, O. Masotta, P. Borrelli, A. M. Owen, A. Estraneo, and A. Soddu, Consciousness and the dimensionality of DOC patients via the generalized Ising model, J. Clin. Med. **9**, 1342 (2020).

[41] P. M. Abeyasinghe, M. Aiello, C. Cavaliere, and A. Owen, A. M. Soddu, A comparison of diffusion tractography techniques in simulating the generalized Ising model to predict the intrinsic activity of the brain, Brain Struct. Funct. **226**, 817 (2021).

[42] H. R. Wilson and J. D. Cowan, Excitatory and inhibitory interactions in localized populations of model neurons, Biophys. J. **12**, 1 (1972).

[43] S. F. Muldoon, F. Pasqualetti, S. Gu, M. Cieslak, S. T. Grafton, J. M. Vettel, and D. S. Bassett, Stimulation-based control of dynamic brain networks, PLoS Comput. Biol. **12**, e1005076 (2016).

[44] A. Lundervold, Consciousness and its measures: Joint workshop for COST actions neuromath and consciousness, Nonlinear Biomed. Phys. **4**, S9 (2010).

[45] K. Bansal, J. D. Medaglia, D. S. Bassett, J. M. Vettel, and S. F. Muldoon, Data-driven brain network models differentiate variability across language tasks, PLoS Comput. Biol. **14**, e1006487 (2018).

[46] K. Bansal, J. Nakuci, and S. F. Muldoon, Personalized brain network models for assessing structure-function relationships, Curr. Opin. Neurobiol. **52**, 42 (2018), systems Neuroscience.

[47] S. G. Waxman and M. V. Bennett, Relative conduction velocities of small myelinated and non-myelinated fibres in the central nervous system, Nat. New Biol. **238**, 217 (1972).

[48] D. Kernell, High-frequency repetitive firing of cat lumbosacral motoneurones stimulated by long-lasting injected currents, Acta Physiol. Scand. **65**, 74 (1965).

[49] W. Rall, Experimental monosynaptic input-output relations in the mammalian spinal cord, J. Cell. Comp. Physiol. **46**, 413 (1955).

[50] In future work, it may be interesting to explore a more general model that incorporates long-range couplings between opposing types of neurons.

[51] See https://www.humanconnectomeproject.org/.

[52] R. S. Desikan, F. Ségonne, B. Fischl, B. T. Quinn, B. C. Dickerson, D. Blacker, R. L. Buckner, A. M. Dale, R. P. Maguire, B. T. Hyman, M. S. Albert, and R. J. Killiany, An automated labeling system for subdividing the human cerebral cortex on MRI scans into gyral based regions of interest, NeuroImage **31**, 968 (2006).

[53] S. Salhi, Y. Kora, G. Ham, H. Z. Haghighi, and C. Simon, Network analysis of the human structural connectome including the brainstem, PLoS ONE **18**, e0272688 (2023).

[54] C. J. Stam and J. C. Reijneveld, Graph theoretical analysis of complex networks in the brain, Nonlinear Biomed. Phys. **1**, 3 (2007).

[55] E. Dijkstra, A note on two problems in connexion with graphs, Numer. Math. **1**, 269 (1959).

[56] N. Meghanathan, Spectral Radius as a Measure of Variation in Node Degree for Complex Network Graphs, *2014 7th International Conference on u- and e- Service* (Science and Technology, Hainan, China, 2014), pp. 30–33.

[57] S. Boccaletti, V. Latora, Y. Moreno, M. Chavez, and D.-U. Hwang, Complex networks: Structure and dynamics, Phys. Rep. **424**, 175 (2006).

[58] M. Barahona and L. M. Pecora, Synchronization in Small-World Systems, Phys. Rev. Lett. **89**, 054101 (2002).

[59] E. Mones, L. Vicsek, and T. Vicsek, Hierarchy measure for complex networks, PLoS ONE **7**, e33799 (2012).

[60] A. A. Hagberg, D. A. Schult, and P. J. Swart, in *Proceedings of the 7th Python in Science Conference*, edited by G. Varoquaux, T. Vaught, and J. Millman, *Exploring Network Structure, Dynamics, and Function using NetworkX* (Pasadena, CA, 2008), pp. 11–15.

[61] J.-P. Onnela, J. Saramäki, J. Kertész, and K. Kaski, Intensity and coherence of motifs in weighted complex networks, Phys. Rev. E **71**, 065103(R) (2005).

[62] We verified the stability of our conclusion against changes to the initial conditions of the oscillators by reconducting the analysis, once with the initial conditions doubled and once with them halved. These changes amounted to a simple shifting of the trend line, but indeed preserved the positive correlation.

[63] E. Bullmore and O. Sporns, The economy of brain network organization, Nat. Rev. Neurosci. **13**, 336 (2012).

[64] D. Meunier, R. Lambiotte, and E. Bullmore, Modular and hierarchically modular organization of brain networks, Front. Neurosci. **4**, 200 (2010).

[65] H.-J. Park and K. Friston, Structural and functional brain networks: From connections to cognition, Science **342**, 1238411 (2013).

[66] P. Moretti and M. Muñoz, Griffiths phases and the stretching of criticality in brain networks, Nat. Commun. **4**, 2521 (2013).

[67] G. Ódor, R. Dickman, and G. Ódor, Griffiths phases and localization in hierarchical modular networks, Sci. Rep. **5**, 14451 (2015).

[68] S. Li, Griffiths phase on hierarchical modular networks with small-world edges, Phys. Rev. E **95**, 032306 (2017).

[69] B. Corominas-Murtra, J. Goñi, R. V. Solé, and C. Rodríguez-Caso, On the origins of hierarchy in complex networks, Proc. Natl. Acad. Sci. USA **110**, 13316 (2013).

[70] T. Nishikawa, A. E. Motter, Y.-C. Lai, and F. C. Hoppensteadt, Heterogeneity in Oscillator Networks: Are Smaller Worlds Easier to Synchronize? Phys. Rev. Lett. **91**, 014101 (2003).

[71] O. Kinouchi and M. Copelli, Optimal dynamical range of excitable networks at criticality, Nat. Phys. **2**, 348 (2006).

[72] L. Cocchi, L. L. Gollo, A. Zalesky, and M. Breakspear, Criticality in the brain: A synthesis of neurobiology, models and cognition, Prog. Neurobiol. **158**, 132 (2017).

[73] M. Yaghoubi, T. de Graaf, J. G. Orlandi, F. Girotto, M. A. Colicos, and J. Davidsen, Neuronal avalanche dynamics indicates different universality classes in neuronal cultures, Sci. Rep. **8**, 3417 (2018).

[74] D. J. Korchinski, J. G. Orlandi, S.-W. Son, and J. Davidsen, Criticality in Spreading Processes without Timescale Separation and the Critical Brain Hypothesis, Phys. Rev. X **11**, 021059 (2021).

[75] D. Curic, V. E. Ivan, D. T. Cuesta, I. M. Esteves, M. H. Mohajerani, A. J. Gruber, and J. Davidsen, Deconstructing scale-free neuronal avalanches: Behavioral transitions and neuronal response, J. Phys. Complex. **2**, 045010 (2021).

[76] S. di Santo, P. Villegas, R. Burioni, and M. A. Muñoz, Landau-Ginzburg theory of cortex dynamics: Scale-free avalanches emerge at the edge of synchronization, Proc. Natl. Acad. Sci. USA **115**, E1356 (2018).

[77] B. J. Baars, Global workspace theory of consciousness: Toward a cognitive neuroscience of human experience, Prog. Brain Res. **150**, 45 (2005).

[78] S. Dehaene, C. Sergent, and J.-P. Changeux, A neuronal network model linking subjective reports and objective physiological data during conscious perception, Proc. Natl. Acad. Sci. USA **100**, 8520 (2003).

[79] G. A. Mashour, P. Roelfsema, J.-P. Changeux, and S. Dehaene, Conscious Processing and the global neuronal workspace hypothesis, Neuron **105**, 776 (2020).

[80] T. Zhao, Y. Zhu, H. Tang, R. Xie, J. Zhu, and J. H. Zhang, Consciousness: New concepts and neural networks, Front. Cell. Neurosci. **13**, 302 (2019).

[81] N. J. M. Popiel, S. Khajehabdollahi, P. M. Abeyasinghe, F. Riganello, E. S. Nichols, A. M. Owen, and A. Soddu, The emergence of integrated information, complexity, and 'consciousness' at criticality, Entropy **22**, 339 (2020).

[82] See https://www.humanconnectome.org/study/hcp-young-adult

[83] See https://github.com/SalmaSalhi7/Structural-Connectome-Project

[84] D. Watts and S. Strogatz, Collective dynamics of 'small-world' networks, Nature (London) **393**, 440 (1998).